Clamping-Layer-Mediated Strain Engineering of Electrical Transport in Freestanding Nickelates Membranes

Huan Ye(叶欢), Fang Xu(许方), Ao Wang(王傲), Yueming Huang(黄悦铭), Jingdi Lu(鲁京迪), Feng Jin(金峰), Wenbin Wu(吴文彬), Jinfeng Zhang(章金凤)*, and Lingfei Wang(王凌飞)*

Hefei National Research Center for Physical Sciences at the Microscale, University of Science and Technology of China, Hefei 230026, China

(Received 17 August 2025; accepted manuscript online 28 September 2025)

Strain engineering serves as an effective approach for tuning the properties of transition metal oxides and their heterostructures. However, conventional epitaxial approaches are fundamentally constrained by the limited choice of substrates, which restricts the ability to achieve continuous strain modulation. The emergence of freestanding oxide thin films has significantly expanded the scope of strain manipulation, allowing the application of larger tensile strains and the induction of novel functionalities. Nevertheless, current freestanding film technologies face a critical limitation: strain modulation has so far been confined to tensile strain, while the application of compressive strain remains inaccessible. To overcome this challenge, we designed a symmetric tri-layer structure composed of clamping layer/nickelate/clamping layer, which enables modulation of the metal-insulator transition in freestanding $NdNiO_3$ and $LaNiO_3$ thin films under both tensile and compressive strain. This clamping-layer-mediated strain engineering approach can be readily generalized to other freestanding oxide systems, providing a versatile platform for manipulating the physical properties of freestanding thin films.

DOI: 10.1088/0256-307X/42/11/110711 CSTR: 32039.14.0256-307X.42.11.110711

Epitaxial strain is one of the most effective methods for modulating the functionalities of transition metal oxide thin films and heterostructures.[1–4] When oxide films are grown epitaxially on various substrates, lattice mismatch induces either biaxial or anisotropic strains.[1,5–7] Owing to the intricate coupling among charge, spin, orbital, and lattice degrees of freedom in transition metal oxides,[8] epitaxial strain can profoundly modulate a wide range of intriguing properties, including metal-insulator transition (MIT),[9–12] magnetic phase separation,[13,14] superconducting transitions,[15] ferroelectric polarization and domain configurations.[16–21] Moreover, recent studies have demonstrated that substantial improvement of ferroelectric and multiferroic properties can be achieved in oxide thin films via the synergistic effect of chemical doping and strain engineering.[22–24] However, the limited selection of substrates confines strain to discrete values, and inevitable strain relaxation processes further restrict the achievable strain to about ±3%.[1,25–28]

Recent advances in freestanding oxide membranes have considerably expanded the strain tunability. By transferring and adhering these membranes onto flexible polymer substrates, extremely large uniaxial strains can be applied by mechanically stretching the freestanding oxide/polymer bilayer. For instance, Hwang *et al.* demonstrated exceptional strain tunability up to 8.0% in freestanding $La_{0.7}Ca_{0.3}MnO_3$ membrane,[29] where such extreme lattice deformation drives a pronounced phase transition from a ferromagnetic metal to an antiferromagnetic insulator. Similarly, freestanding $SrTiO_3$ (STO) thin films have been shown to sustain uniaxial tensile strains exceeding 2.0%,[30] enabling continuous tuning of ferroelectric properties.[16] In addition, Chen *et al.* reported uniaxial strains up to 5.1% in freestanding $BiMnO_3$ membranes, with robust ferroelectricity confirmed under 1.7% tensile strain.[31] Collectively, these advances highlight the exceptional potential of freestanding oxide membranes to surpass the traditional limits of epitaxial strain. Nevertheless, it should be emphasized that flexible substrate-assisted strain engineering can only impose tensile strain on the oxide membranes, leaving compressive strain inaccessible and posing a critical limitation for fully tuning their physical properties.

Previous studies have shown that thin buffer or capping layers (the so-called "clamping layers") can effectively suppress interdiffusion during growth and improve the crystallinity of freestanding oxide membranes.[32] Meanwhile, when interfacial lattice mismatch exists, these clamping layers can also impose considerable epitaxial strain on the released membranes. Building on this concept, we use perovskite-structured nickelates as a model system and introduce a clamping-layer-mediated approach for applying both tensile and compressive strain to freestanding oxide membranes. As illustrated in Figs. 1(a)–1(c), sandwiching the $LnNiO_3$ nickelate layer between two perovskite oxide clamping layers [STO or $LaAlO_3$ (LAO)] generates significant strain through lattice mismatch at the heterointerfaces. Furthermore, the magnitude of strain

*Corresponding authors. Email: zjinfeng@ustc.edu.cn; wanglf@ustc.edu.cn
© 2025 Chinese Physical Society and IOP Publishing Ltd. All rights, including for text and data mining, AI training, and similar technologies, are reserved.

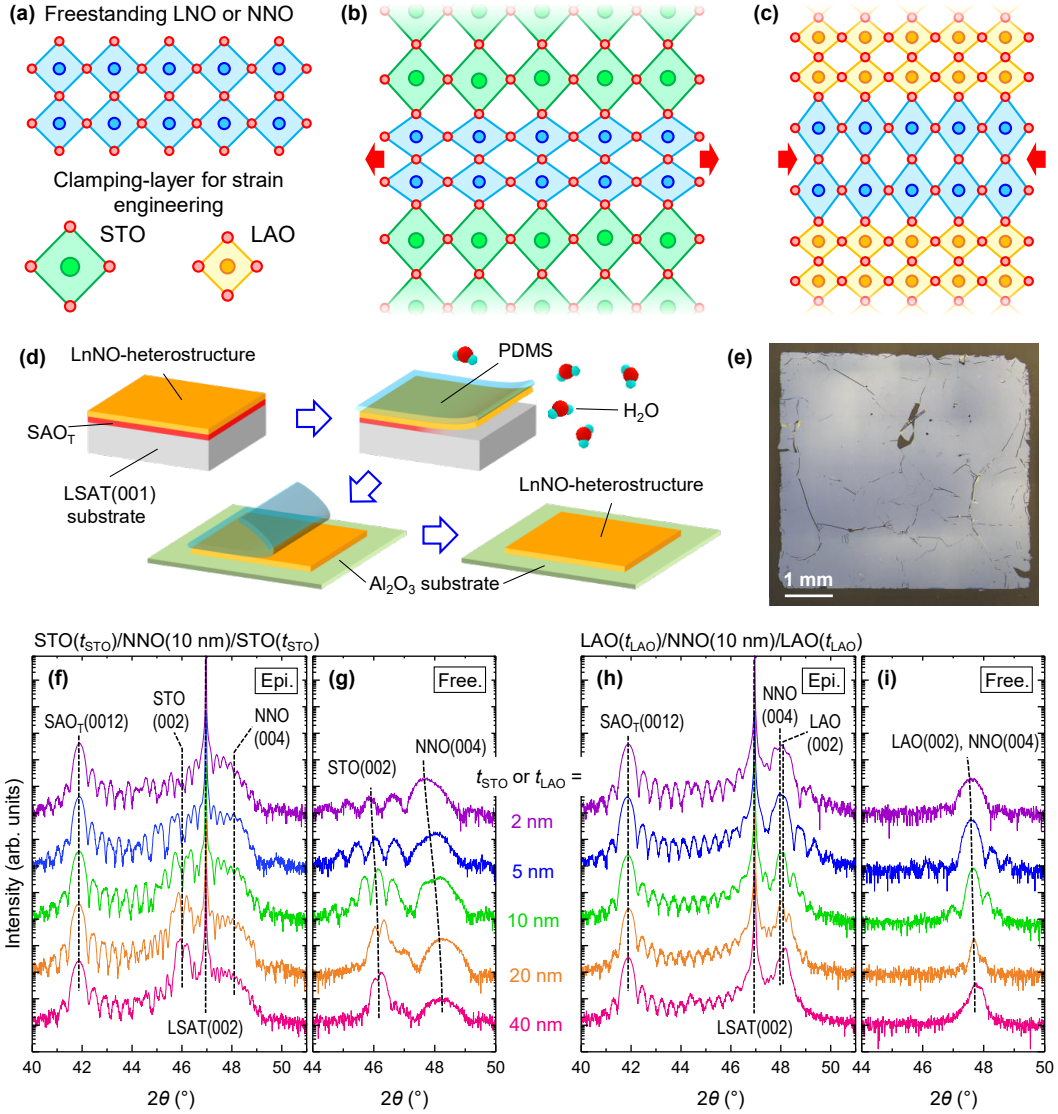

Fig. 1. Clamping-layer-mediated strain engineering and preparation of freestanding nickelate membranes. (a)–(c) Schematic illustrations of tensile and compressive strain engineering in freestanding $LnNiO_3$ (LnNO, where Ln = Nd or La, denoted as NNO and LNO, respectively) membranes mediated by clamping layers. (d) Schematic illustration of the water-release and transfer procedures of LnNO-based freestanding membranes. (e) Optical micrograph of a representative 10-nm-thick freestanding NNO film after transfer. (f) and (h) XRD 2θ–ω scans of STO(t_{STO})/NNO(10 nm)/STO(t_{STO}) and LAO(t_{LAO})/NNO(10 nm)/LAO(t_{LAO}) tri-layer epitaxially grown on SAO_T/LSAT(001). From top to bottom, the curves correspond to STO or LAO clamping layers with sequentially increasing thicknesses of 2, 5, 10, 20, and 40 nm. (g) and (i) XRD 2θ–ω scans of the STO(t_{STO})/NNO(10 nm)/STO(t_{STO}) and LAO(t_{LAO})/NNO(10 nm)/LAO(t_{LAO}) tri-layer heterostructures transferred onto Al_2O_3(001) substrates after water release.

can be continuously tuned by varying the thicknesses of the clamping layers. This clamping-layer-mediated strain engineering offers an effective means of tailoring the electronic and structural properties of freestanding nickelate thin films, particularly in controlling metallicity and MIT. Beyond nickelates, this experimentally accessible approach can be readily extended to other freestanding oxide heterostructures, offering new opportunities for tuning physical properties and advancing flexible electronic devices.

We selected STO and LAO as clamping-layer materials to impose symmetric, biaxial misfit strain on freestanding $LnNiO_3$ (LnNO, where Ln = Nd or La, denoted as NNO and LNO, respectively) membranes. The pseudo-cubic lattice parameters (a_p) of bulk NNO, LNO, STO, and LAO are 3.81 Å, 3.859 Å, 3.905 Å, and 3.789 Å, respectively. Thus, epitaxially stacking the STO or LAO clamping layers with the LnNO layer is expected to induce tensile or compressive strains [Figs. 1(a)–1(c)]. Accordingly, we deposited the STO/LnNO(10 nm)/STO and LAO/LnNO(10 nm)/LAO tri-layer heterostructures using a custom-built pulsed laser deposition chamber equipped with a KrF excimer laser (λ = 248 nm). By controlling deposition durations, the thicknesses of the STO and LAO layers (denoted as t_{STO} and t_{LAO}) were varied from 2 to 40 nm. All tri-layers were epitaxially grown on (001)-oriented $(LaAlO_3)_{0.3}$-$(SrAl_{0.5}Ta_{0.5}O_3)_{0.7}$ [LSAT (001)] substrates buffered with a 20 nm-thick water-soluble $Sr_4Al_2O_7$

(SAO_T) sacrificial layer. X-ray diffraction (XRD) 2θ–ω linear scans of the STO/NNO/STO/SAO_T/LSAT(001) and LAO/NNO/LAO/SAO_T/LSAT(001) heterostructures [Figs. 1(f) and 1(h)] display well-defined NNO(004) and SAO_T(0012) diffraction peaks. The intensity of the clamping-layer peak [STO(002) or LAO(002)] systematically increases with t_{STO} or t_{LAO}. The presence of sharp Laue fringes near these peaks indicates excellent crystallinity of the heterostructures, likely attributed to the strong structural coherence enabled by the SAO_T layer.[33,34]

The freestanding tri-layer oxide membranes were prepared through standard polymer-assisted procedures [Fig. 1(d)]: Polydimethylsiloxane (PDMS) was first attached to the heterostructure, after which the entire sample was immersed in deionized (DI) water. Dissolution of the SAO_T sacrificial layer released the freestanding membranes from the LSAT(001) substrates, enabling their transfer onto the Al_2O_3(001) substrates. Benefiting from the superior water solubility of SAO_T and the high crystallinity of the tri-layer epitaxial heterostructures, the water-released STO/NNO/STO and LAO/NNO/LAO membranes contained millimeter-sized crack-free regions, sufficient for subsequent structural and electrical characterizations. The 2θ–ω linear scans of the freestanding heterostructures [Figs. 1(g) and 1(i)] show high-intensity NNO(004) diffraction peaks, confirming the preservation of high crystallinity after water release. Consistent results were obtained from XRD measurements of LNO-based tri-layer heterostructures, which also showed structural integrity before and after water release [Fig. S1 of the Supplementary Materials (SM)].

To characterize the strain states imposed by clamping layers on the NNO and LNO layers, we conducted reciprocal space mapping (RSM) characterizations on both epitaxial and freestanding tri-layer heterostructures. The RSMs around the LSAT(103) diffraction [Figs. 2(a), 2(f) and Fig. S2 of the SM] suggest coherent strain in the epitaxially grown STO/LnNO/STO and LAO/LnNO/LAO heterostructures, as the diffraction spots share identical in-plane reciprocal space vectors (Q_x). After water release and transfer onto Al_2O_3(001) substrates, the Q_x (Q_z) values of the LnNO(116) reflections in the RSMs of the freestanding STO/LnNO/STO heterostructures gradually decrease (increase) with increasing t_{STO} [Figs. 2(b)–2(d) and Fig. S3 of the SM]. From the RSMs, we extracted the in-plane lattice constant of LnNO (a_{LnNO}, in pseudocubic notation) [Fig. 2(e) and Fig. S3 of the SM]. a_{LnNO} initially increases linearly with t_{STO} before saturating at ~3.91 Å, close to the in-plane lattice constant of STO.

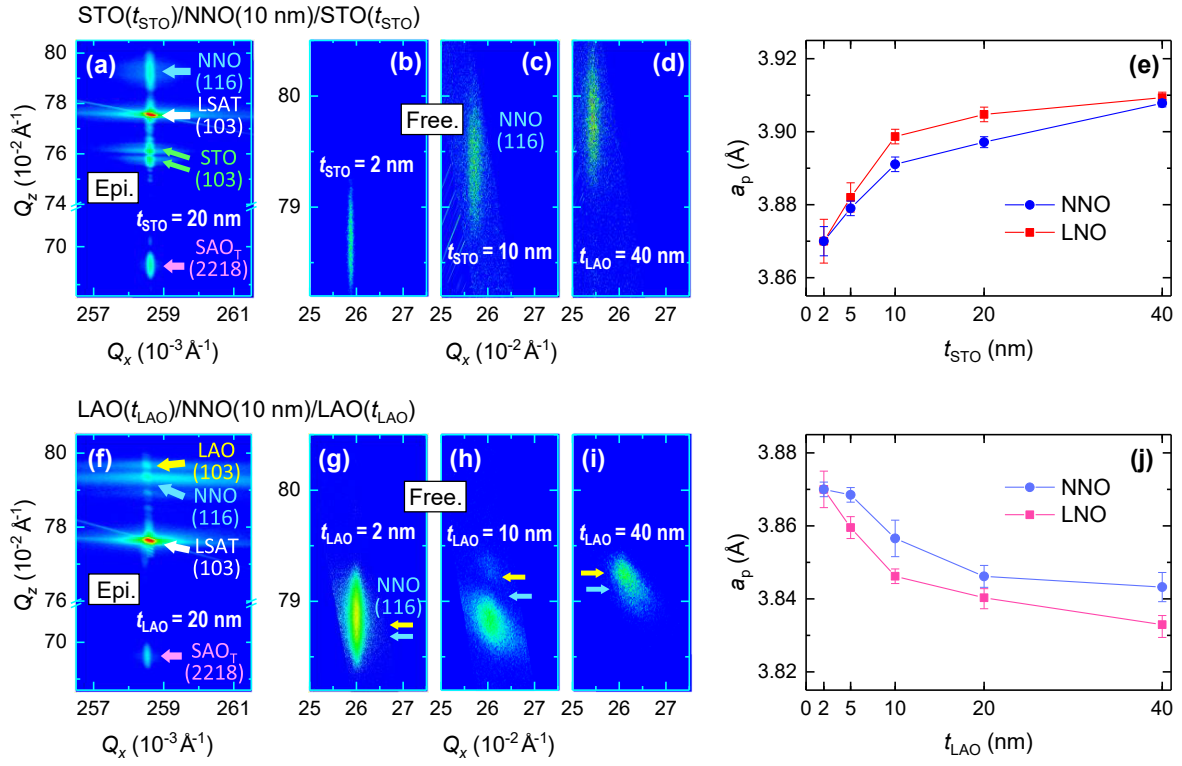

Fig. 2. RSM characterizations of the as-grown and transferred NNO-heterostructures. (a) RSM around the LSAT(103) diffraction measured for the epitaxial STO(20 nm)/NNO(10 nm)/STO(20 nm)/SAO_T/LSAT(001) heterostructure. (b)–(d) RSMs around the NNO(116) reflection for STO(t_{STO})/NNO(10 nm)/STO(t_{STO}) freestanding tri-layer heterostructures transferred onto the Al_2O_3(001) substrates. (e) In-plane lattice constants of NNO and LNO layers (pseudocubic notation, a_p) as a function of t_{STO}. (f) RSM spectra around LSAT(103) reflection measured for the LAO(20 nm)/NNO(10 nm)/LAO(20 nm)/SAO_T/LSAT(001) heterostructure. (g)–(i) RSMs around the NNO(116) asymmetric reflection for LAO(t_{LAO})/NNO(10 nm)/LAO(t_{LAO}) heterostructures transferred onto Al_2O_3(001) substrates. With increasing t_{LAO}, the Q_x value of NNO gradually increases, indicating a progressively stronger in-plane compressive strain. (j) In-plane lattice constants of NNO and LNO as a function of t_{LAO} for LAO(t_{LAO})/LnNO(10 nm)/LAO(t_{LAO}) freestanding membranes transferred onto Al_2O_3(001) substrates. Error bars in (e) and (j) represent the fitting uncertainty of the lattice constants.

Concurrently, c_{LnNO} decreases and then saturates with increasing t_{STO}. The simultaneous in-plane expansion and out-of-plane contraction further corroborate that the STO clamping layers indeed impose a tunable biaxial tensile strain on the NNO and LNO layers. For the freestanding LAO/LnNO/LAO heterostructures transferred onto $Al_2O_3(001)$ substrates, the Q_x values of LnNO(116) reflections gradually increase with t_{LAO} [Figs. 2(g)–2(i) and Fig. S3 of the SM]. Correspondingly, a_{LnNO} decreases linearly with t_{LAO} before tending toward saturation at ∼3.84 Å. These results suggest that LAO clamping layers impose a tunable biaxial compressive strain on LNO and NNO layers. In contrast to STO/LnNO/STO cases, however, changes in c_{LnNO} for LAO/LnNO/LAO heterostructures are negligible (Fig. S4 of the SM). This trend strongly suggests that LnNO layers accommodate compressive strain primarily by increasing out-of-plane octahedral rotation angle rather than by directly shortening in-plane Ni-O bonds.[35,36]

Bulk NNO is well-known for exhibiting a pronounced MIT at approximately 190 K.[37,38] To investigate how STO and LAO clamping layers affect this MIT, we measured temperature-dependent resistivity (ρ–T) curves for a series of the freestanding STO/NNO/STO and LAO/NNO/LAO tri-layers with varying t_{STO} and t_{LAO} [Figs. 3(a) and 3(b)]. Interestingly, the critical MIT temperature (T_{MI}) changes only slightly in both tri-layer heterostructures, while the room-temperature metallicity and the magnitude of MIT vary significantly. To clarify the evolution of MIT due to the clamping layers, we plot the ρ at 300 K ($\rho_{300\,\mathrm{K}}$, reflecting metallicity at room temperature) and the ρ ratio $\rho_{10\,\mathrm{K}}/\rho_{300\,\mathrm{K}}$ (indicating the MIT magnitude) in Figs. 3(c) and 3(d), respectively. Compared with the 10 nm NNO single-layer film (Fig. S5 of the SM), the freestanding STO/NNO/STO tri-layer with t_{STO} = 2 nm shows a slight enhancement in the MIT amplitude, which can be attributed to reduced structural disorder under weak tensile strain. Increasing t_{STO} to 5 nm results in a slight decrease in $\rho_{300\,\mathrm{K}}$ and an order of magnitude increase in $\rho_{10\,\mathrm{K}}/\rho_{300\,\mathrm{K}}$, reflecting a pronounced enhancement of MIT. With further increases in t_{STO} from 10 to 40 nm, $\rho_{300\,\mathrm{K}}$ rises monotonically, whereas the $\rho_{10\,\mathrm{K}}/\rho_{300\,\mathrm{K}}$ ratio remains nearly unchanged. Hence, STO-imposed tensile strain can suppress room-temperature metallicity without significantly affecting the magnitude of MIT. As shown by strain analyses in Fig. 2, NNO layer accommodates tensile strain primarily by elongating Ni-O bonds, which weakens hybridization between Ni 3d and O 2p orbitals and thereby suppresses metallicity. Nevertheless, this structural modification does not hinder Ni-O bond disproportionation upon cooling, leaving magnitude of MIT largely unaffected.[9]

Similarly, the compressive strain imposed by the LAO clamping layers can also strongly modulate the MIT of the freestanding LAO/NNO/LAO tri-layers. As t_{LAO} increases from 2 to 40 nm, $\rho_{300\,\mathrm{K}}$ increases monotonically, but the increment is smaller than in the STO/NNO/STO case, suggesting that compressive strain is less effective at weakening the room-temperature metallicity of NNO.

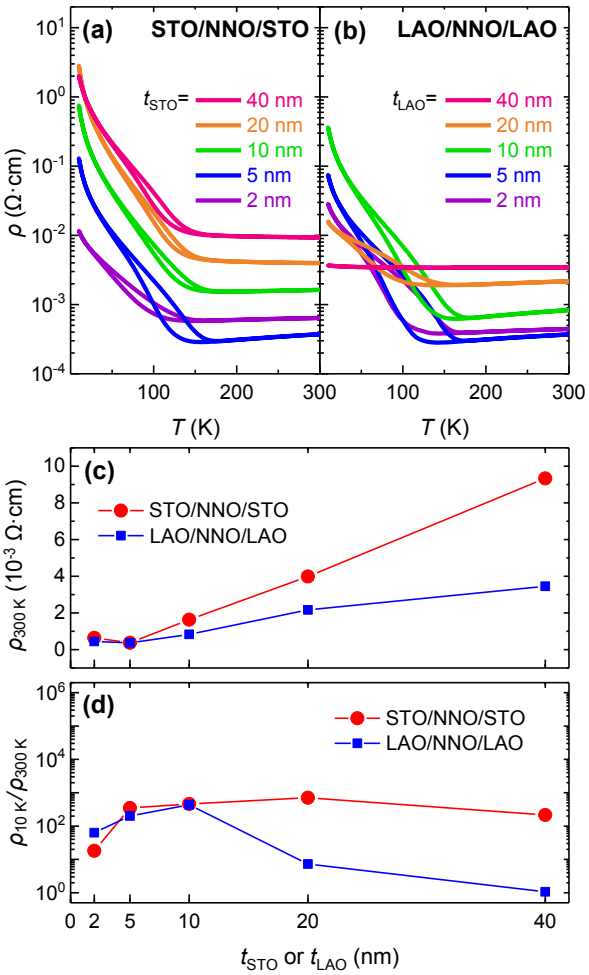

Fig. 3. Transport measurements of $NdNiO_3$-heterostructures transferred onto $Al_2O_3(001)$ substrates. (a) and (b) Temperature-dependent resistivity (ρ–T) of STO(t_{STO})/NNO(10 nm)/STO(t_{STO}) and LAO(t_{LAO})/NNO(10 nm)/LAO(t_{LAO}) heterostructures with varying STO and LAO layer thicknesses (t_{STO} and t_{LAO}). (c) Resistivity at 300 K ($\rho_{300\,\mathrm{K}}$) and (d) the resistivity ratio $\rho_{10\,\mathrm{K}}/\rho_{300\,\mathrm{K}}$ as functions of t_{STO} and t_{LAO}, extracted from the ρ–T curves of the STO(t_{STO})/NNO(10 nm)/STO(t_{STO}) and LAO(t_{LAO})/NNO(10 nm)/LAO(t_{LAO}) freestanding tri-layer heterostructures. Here, $\rho_{300\,\mathrm{K}}$ represents the room-temperature resistivity, while the ratio $\rho_{10\,\mathrm{K}}/\rho_{300\,\mathrm{K}}$ quantifies the magnitude of the MIT.

More intriguingly, the $\rho_{10\mathrm{K}}/\rho_{300\mathrm{K}}$ ratio exhibits a distinct non-monotonic dependence on t_{LAO}. As t_{LAO} increases from 2 to 10 nm, the ratio increases linearly with t_{LAO}, likely due to improved crystallinity and modest enhancement of Ni-O bond disproportionation under compressive strain. As t_{LAO} increases from 2 to 10 nm, the observed enhancement of MIT may correspond to strain-reduced structural disorder. Upon further increasing t_{LAO} to 20 and 40 nm, the $\rho_{10\,\mathrm{K}}/\rho_{300\,\mathrm{K}}$ ratio decreases dramatically by nearly two orders of magnitude, signifying a substantial MIT suppression. Especially for the t_{LAO} = 40 nm case, the MIT vanishes entirely in the ρ–T curve [Fig. 3(b)]. This behavior can be understood as a consequence of progressively intensified compressive strain, which reduces the in-plane lattice constant while straightening out-of-plane

Ni-O-Ni bond angle toward 180°. These structural modifications enhance the Ni 3d-O 2p orbital hybridization, thereby broadening the effective electronic bandwidth. As compressive strain increases, the bandwidth approaches or even exceeds the charge-transfer energy, weakening the charge ordering responsible for the insulating phase and stabilizing the metallic state. Consequently, both T_{MI} and the MIT magnitude progressively diminish and eventually disappear.[10,39] This trend is consistent with previously reported transport properties of epitaxial NNO films under compressive strain[40–42] as well as bulk compounds under hydrostatic pressure.[43,44] Together with the structural analyses, these results suggest that compressive strain-induced enhancement of out-of-plane octahedral rotations effectively hinders Ni-O bond disproportionation and associated charge disproportionation, thus quenching the MIT.

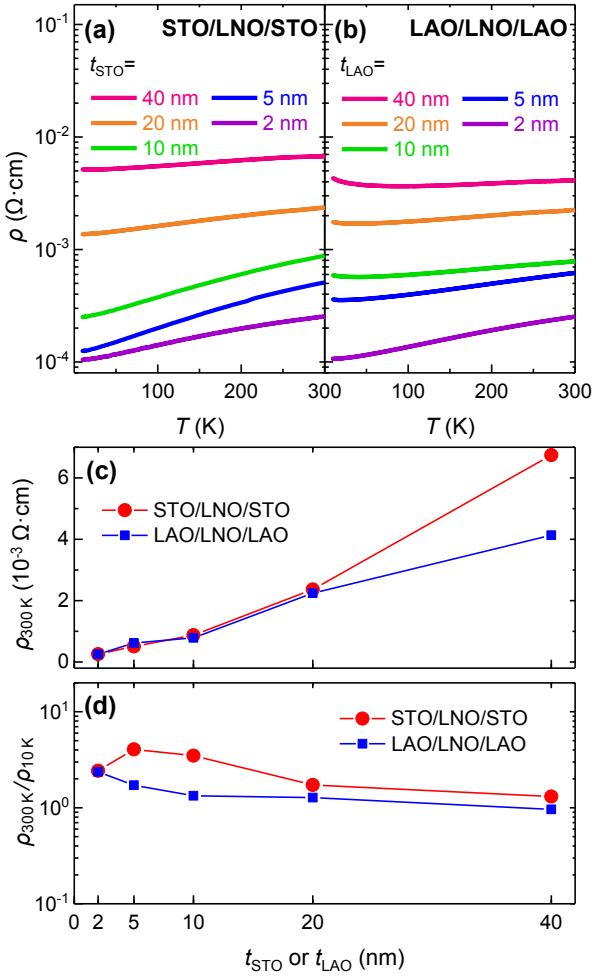

Fig. 4. Transport properties of $LaNiO_3$-heterostructures transferred onto Al_2O_3(001) substrates. (a) and (b) ρ–T curves of STO(t_{STO})/LNO(10 nm)/STO(t_{STO}) and LAO(t_{LAO})/LNO(10 nm)/LAO(t_{LAO}) heterostructures with varying t_{STO} and t_{LAO}. (c) $\rho_{300\,\mathrm{K}}$ and (d) resistivity ratio $\rho_{300\,\mathrm{K}}/\rho_{10\,\mathrm{K}}$ as functions of t_{STO} and t_{LAO}, extracted from the ρ–T curves of the STO(t_{STO})/LNO(10 nm)/STO(t_{STO}) and LAO(t_{LAO})/LNO(10 nm)/LAO(t_{LAO}) freestanding tri-layer heterostructures. The $\rho_{300\,\mathrm{K}}/\rho_{10\,\mathrm{K}}$ ratio reflects the low-temperature resistivity upturn, with smaller values indicating a more obvious insulating behavior.

Unlike bulk NNO, which undergoes a MIT, bulk LNO is intrinsically a correlated metal whose metallicity can also be modulated via epitaxial strain.[45,46] Figure 4 summarizes the ρ–T curves of the STO/LNO/STO and LAO/LNO/LAO freestanding tri-layers [Figs. 4(a) and 4(b)]. In the high-temperature regime, all ρ–T curves exhibit a monotonic decrease in ρ upon cooling, signifying robust metallicity. The dependence of $\rho_{300\mathrm{K}}$ on t_{STO} and t_{LAO} is shown in Fig. 4(c). Similar to the NNO-based tri-layer, $\rho_{300\mathrm{K}}$ increases monotonically with t_{STO} and t_{LAO}, demonstrating that both tensile and compressive strain degrade metallicity. Moreover, as shown in Fig. 4(a), STO/LNO/STO freestanding tri-layers with $t_{\mathrm{STO}} \leq 10$ nm retain metallic behavior over the entire T range down to 10 K. In contrast, thicker clamping layers ($t_{\mathrm{STO}} > 10$ nm) result in a slight increase in ρ at low temperature, a feature previously ascribed to a complex interplay of weak localization and electron–electron interaction.[47] The low-temperature insulating tendency becomes more pronounced in LAO/LNO/LAO freestanding tri-layers [Fig. 4(b)]. For $t_{\mathrm{LAO}} = 5$ nm, the ρ–T curve already exhibits weak insulating behavior below ∼18 K, and as t_{LAO} increases to 40 nm, the ρ upturn becomes much stronger, occurring at ∼70 K. This trend is further quantified in Fig. 4(d), where the $\rho_{300\mathrm{K}}/\rho_{10\mathrm{K}}$ ratio decreases systematically, with smaller values corresponding to a stronger low-temperature upturn. For the STO/LNO/STO freestanding tri-layers, tensile strain from the STO clamping layers significantly elongates the Ni-O bonds, weakening Ni 3d-O 2p orbital hybridization and thereby triggering insulating behavior at low temperatures. In contrast, for the LAO/LNO/LAO freestanding tri-layers, compressive strain shortens the in-plane Ni-O bond length, which should, in principle, favor metallicity. However, the associated in-plane oxygen octahedral rotations reduce the Ni-O-Ni bond angle from 180°, suppressing electron hopping. The resulting enhancement of electronic localization ultimately drives the low-temperature insulating behavior.[35]

In summary, we have demonstrated an innovative strain-engineering strategy for freestanding oxide membranes by employing perovskite oxide clamping layers to impose controlled tensile and compressive strains. Using NNO and LNO as model systems, we systematically examined how varying the composition and thickness of STO and LAO clamping layers modulates structural and electronic properties, particularly influencing the MIT and correlated metallic states. Importantly, this clamping-layer-mediated approach is broadly applicable beyond nickelates, providing a versatile platform for tailoring the functionalities of other freestanding oxide membranes with diverse physical properties. For example, in ferromagnetic system such as $(La,Sr)MnO_3$ or $SrRuO_3$, strain tuning can precisely control magnetic anisotropy and Curie temperatures.[48,49] Similarly, in ferroelectric system such as $BaTiO_3$ or $Pb(Zr,Ti)O_3$, this method can enhance spontaneous polarization or stabilize exotic polar states—including polar vortices[50] and skyrmions[51]—through carefully tuned compressive or tensile strain. Overall, our

work establishes clamping-layer-mediated strain engineering as a powerful and widely applicable strategy for exploring and optimizing novel functionalities in freestanding oxide thin films, paving the way for next-generation oxide-based electronic, magnetic, and ferroelectric devices.

Materials and Methods.

1. Synthesis of the Polycrystalline Ceramic Target and Epitaxial Films. The NNO and $Sr_3Al_2O_6$ (SAO) bulk targets were synthesized using the solid-state reaction method. Powders of Nd_2O_3 and NiO were weighed in stoichiometric ratios, thoroughly ground, and then calcined at 1200 ℃ and 1300 ℃ for 12 h each. The resulting mixture was pressed into pellets and sintered at 1350 ℃ for an additional 12 h to obtain the NNO polycrystalline target. Similarly, SAO or STO targets were prepared by reacting Al_2O_3 or TiO_2 with $SrCO_3$ under the same procedure.

In this study, NNO, LNO, SAO, STO, and LAO thin films were deposited on LSAT(001) single-crystal substrates utilizing pulsed laser deposition with a KrF excimer laser ($\lambda = 248$ nm). The laser energy densities used for ablating the NNO (or LNO), SAO, STO, and LAO targets were approximately 2 J/cm^2, 1 J/cm^2, 1.5 J/cm^2, and 1.6 J/cm^2, respectively. The substrate temperatures during deposition were maintained at 700 ℃, 840 ℃, 840 ℃, and 730 ℃, respectively. Additionally, the oxygen partial pressures were set to 20 Pa, 5 Pa, 5 Pa, and 15 Pa, respectively. The distance between the target and the substrate was fixed at 50 mm for all depositions. Following the deposition procedures, the films were annealed *in situ* under the growth conditions for 10 minutes and then cooled to room temperature.

2. Transfer of Freestanding Membranes. A flexible polymer support PDMS was first attached to the surface of the as-grown LnNO-heterostructure [Fig. 1(d)]. The PDMS/heterostructure assembly was then immersed in room-temperature DI water to dissolve the underlying SAO_T sacrificial layer. Once dissolution was complete, the freestanding membrane was transferred onto an $Al_2O_3(001)$ substrate by gently pressing the PDMS-supported membrane onto the substrate heated to 80 ℃. Finally, the PDMS support was peeled off, leaving a clean, freestanding membrane adhered to the $Al_2O_3(001)$ substrate.

3. Structural and Electrical Characterizations. The high-quality epitaxial structures of STO(t_{STO})-LnNiO(10 nm)-STO(t_{STO}) and $LaAlO_3$(t_{LAO})-LnNiO (10 nm)-$LaAlO_3$(t_{LAO}) (where Ln = Nd and La) tri-layer films were characterized by X-ray diffraction (XRD, PANalytical Empyrean X-ray diffractometer, Cu $K_{\alpha 1}$ radiation) with both 2θ–ω line scan and off-specular RSM.

Longitudinal resistance measurements were characterized by using a physical properties measurement system (PPMS-14T, Quantum Design) over the temperature range of 10–300 K with a cooling/warming rate of 2 K/min. A linear four-point geometry with Pt top electrodes was employed to ensure Ohmic contacts. For these measurements, the film samples were patterned into Hall bars with dimensions on the order of hundreds of micrometers using photolithography.

Acknowledgements. This work was supported by the National Key Research and Development Program of China (Grant No. 2023YFA1406404), the National Natural Science Foundation of China (Grant Nos. 12504152, 52572144, 12374094, and 12074365), China Postdoctoral Science Foundation (Grant No. 2024M763130), the China Postdoctoral Science Foundation-Anhui jointSupport Program (Grant No. 2024T007AH), the Fundamental Research Funds for the Central Universities (Grant No. WK9990000158), Chinese Academy of Sciences Project for Young Scientists in Basic Research (Grant No. YSBR-084), Innovation Program for Quantum Science and Technology (Grant No. 2024ZD0301300), and Anhui Provincial Natural Science Foundation (Grant No. 2308085MA15). The sample fabrication was partially carried out at the University of Science and Technology of China (USTC) Center for Micro and Nanoscale Research and Fabrication. And the electrical characterizations were carried out at Instruments Center for Physical Science, USTC.

References

[1] Schlom D G, Chen L Q, Fennie C J, Gopalan V, Muller D A, Pan X, Ramesh R, and Uecker R 2014 *MRS Bull.* **39** 118
[2] Jia Y, Liang Z, Pan H, Wang Q, Lv Q, Yan Y, Jin F, Hou D, Wang L, and Wu W 2023 *Chin. Phys. B* **32** 027501
[3] Wei Y, Nukala P, Salverda M, Matzen S, Zhao H J, Momand J, Everhardt A S, Agnus G, Blake G R, Lecoeur P, Kooi B J, Íñiguez J, Dkhil B, and Noheda B 2018 *Nat. Mater.* **17** 1095
[4] Zhang L, Chen J, Fan L, Diéguez O, Cao J, Pan Z, Wang Y, Wang J, Kim M, Deng S, Wang J, Wang H, Deng J, Yu R, Scott J F, and Xing X 2018 *Science* **361** 494
[5] Locquet J P, Perret J, Fompeyrine J, Mächler E, Seo J W, and Van Tendeloo G 1998 *Nature* **394** 453
[6] Bozovic I, Logvenov G, Belca I, Narimbetov B, and Sveklo I 2002 *Phys. Rev. lett.* **89** 107001
[7] Gan Q, Rao R A, Eom C B, Garrett J L, and Lee M 1998 *Appl. Phys. Lett.* **72** 978
[8] Hwang H Y, Iwasa Y, Kawasaki M, Keimer B, Nagaosa N, and Tokura Y 2012 *Nat. Mater.* **11** 103
[9] Liu J, Kargarian M, Kareev M, Gray B, Ryan P J, Cruz A, Tahir N, Chuang Y-D, Guo J, Rondinelli J M, Freeland J W, Fiete G A, and Chakhalian J 2013 *Nat. Commun.* **4** 2714
[10] Catalano S, Gibert M, Bisogni V, Peil O E, He F, Sutarto R, Viret M, Zubko P, Scherwitzl R, Georges A, Sawatzky G A, Schmitt T, and Triscone J M 2014 *APL Mater.* **2** 116110
[11] Catalano S, Gibert M, Fowlie J, Íñiguez J, Triscone J M, and Kreisel J 2018 *Rep. Pro. Phys.* **81** 046501
[12] Ye H, Hua E, Xu F, Lu J, Jin F, Wu W, Si L, and Wang L 2024 *Chin. Phys. Lett.* **41** 117301
[13] Lai K, Nakamura M, Kundhikanjana W, Kawasaki M, Tokura Y, Kelly M A, and Shen Z X 2010 *Science* **329** 190
[14] Zhou H, Wang L, Hou Y, Huang Z, Lu Q, and Wu W 2015 *Nat. Commun.* **6** 8980
[15] Hicks C W, Brodsky D O, Yelland E A, Gibbs A S, Bruin J A N, Barber M E, Edkins S D, Nishimura K, Yonezawa S, Maeno Y, and Mackenzie A P 2014 *Science* **344** 283

[16] Haeni J H, Irvin P, Chang W, Uecker R, Reiche P, Li Y L, Choudhury S, Tian W, Hawley M E, Craigo B, Tagantsev A K, Pan X Q, Streiffer S K, Chen L Q, Kirchoefer S W, Levy J, and Schlom D G 2004 *Nature* **430** 758

[17] Liu K, Liu K, Zhang X, Fang J, Jin F, Wu W, Ma C, and Wang L 2024 *Chin. Phys. Lett.* **41** 117701

[18] Choi W, Park B, Hwang J, Han G, Yang S, Lee H, Lee S, Jo J, Borisevich A Y, and Jeong H 2024 *Chin. Phys. B* **33** 096805

[19] Kim Y S, Choi J S, Kim J, Moon S J, Park B H, Yu J, Kwon J H, Kim M, Chung J S, Noh T W, and Yoon J G 2010 *Appl. Phys. Lett.* **97** 242907

[20] Liu K, Jin F, Zhang X, Liu K, Zhang Z, Hua E, Zhang J, Ye H, Gao G, Ma C, Wang L, and Wu W 2023 *Adv. Funct. Mater.* **33** 2209925

[21] De A R, Jung M H, Kim Y H, Bae S B, Jeong S G, Oh J Y, Choi Y, Lee H, Kim Y, Choi T, Kim Y M, Yang S M, Jeong H Y, and Choi W S 2024 *ACS Appl. Mater. Interfaces* **16** 27532

[22] Wang T, Gong F, Ma X, Pan S, Wei X K, Kuo C, Yoshida S, Ku Y C, Wang S, Yang Z, Hazra S, Zhang K H L, Liu X, Tang Y, Zhu Y L, Chang C F, Das S, Ma X, Chen L, Xu B, Gopalan V, Bellaiche L, Martin L W, and Chen Z 2025 *Sci. Adv.* **11** eads8830

[23] Wang T, Zou M J, Zhang D, Ku Y C, Zheng Y, Pan S, Ren Z, Xu Z, Huang H, Luo W, Tang Y, Chen L, Liu C E, Chang C F, Das S, Bellaiche L, Yang Y, Ma X L, Kuo C Y, Liu X, and Chen Z 2025 *Matter* **8** 101874

[24] Damodaran A R, Breckenfeld E, Chen Z, Lee S, and Martin L W 2014 *Adv. Mater.* **26** 6341

[25] Adamo C, Ke X, Wang H Q, Xin H L, Heeg T, Hawley M E, Zander W, Schubert J, Schiffer P, Muller D A, Maritato L, and Schlom D G 2009 *Appl. Phys. Lett.* **95** 112504

[26] Béa H, Dupé B, Fusil S, Mattana R, Jacquet E, Warot-Fonrose B, Wilhelm F, Rogalev A, Petit S, Cros V, Anane A, Petroff F, Bouzehouane K, Geneste G, Dkhil B, Lisenkov S, Ponomareva I, Bellaiche L, Bibes M, and Barthélémy A 2009 *Phys. Rev. Lett.* **102** 217603

[27] Infante I C, Lisenkov S, Dupé B, Bibes M, Fusil S, Jacquet E, Geneste G, Petit S, Courtial A, Juraszek J, Bellaiche L, Barthélémy A, and Dkhil B 2010 *Phys. Rev. Lett.* **105** 057601

[28] Chen Z, Luo Z, Huang C, Qi Y, Yang P, You L, Hu C, Wu T, Wang J, Gao C, Sritharan T, and Chen L 2011 *Adv. Funct. Mater.* **21** 133

[29] Hong S S, Gu M, Verma M, Harbola V, Wang B Y, Lu D, Vailionis A, Hikita Y, Pentcheva R, Rondinelli J M, and Hwang H Y 2020 *Science* **368** 71

[30] Xu R, Huang J, Barnard E S, Hong S S, Singh P, Wong E K, Jansen T, Harbola V, Xiao J, Wang B Y, Crossley S, Lu D, Liu S, and Hwang H Y 2020 *Nat. Commun.* **11** 3141

[31] Jin C, Zhu Y, Li X, An F, Han W, Liu Q, Hu S, Ji Y, Xu Z, Hu S, Ye M, Zhong G, Gu M, and Chen L 2021 *Adv. Sci.* **8** 2102178

[32] Chen Z Y, Wang B Y, Goodge B H, Lu D, Hong S S, Li D F, Kourkoutis, L F, Hikita Y, and Hwang H Y 2019 *Phys. Rev. Mater.* **3** 060801(R)

[33] Zhang J, Lin T, Wang A, Wang X, He Q, Ye H, Lu J, Wang Q, Liang Z, Jin F, Chen S, Fan M, Guo E J, Zhang Q, Gu L, Luo Z, Si L, Wu W, and Wang L 2024 *Science* **383** 388

[34] Nian L, Sun H, Wang Z, Xu D, Hao B, Yan S, Li Y, Zhou J, Deng Y, Hao Y, and Nie Y 2024 *Adv. Mater.* **36** 2307682

[35] Fowlie J, Lichtensteiger C, Gibert M, Meley H, Willmott P, and Triscone J M 2019 *Nano Lett.* **19** 4188

[36] Anada M, Kowa K, Maeda H, Sakai E, Kitamura M, Kumigashira H, Sakata O, Nakanishi-Ohno Y, Okada M, Kimura T, and Wakabayashi Y 2018 *Phys. Rev. B* **98** 014105

[37] Catalan G 2008 *Phase Trans.* **81** 729

[38] Eguchi R, Okamoto Y, Hiroi Z, Shin S, Chainani A, Tanaka Y, Matsunami M, Takata Y, Nishino Y, Tamasaku K, Yabashi M, and Ishikawa T 2009 *J. Appl. Phys.* **105** 056103

[39] Wang L, Ju S, You L, Qi Y, Guo Y W, Ren P, Zhou Y, and Wang J 2015 *Sci. Rep.* **5** 18707

[40] Xiang P H, Zhong N, Duan C G, Tang X D, Hu Z G, Yang P X, Zhu Z Q, and Chu J H 2013 *J. Appl. Phys.* **114** 243713

[41] Scherwitzl R, Zubko P, Lezama I G, Ono S, Morpurgo A F, Catalan G, and Triscone J 2010 *Adv. Mater.* **22** 5517

[42] Disa A S, Kumah D P, Ngai J H, Specht E D, Arena D A, Walker F J, and Ahn C H 2013 *APL Mater.* **1** 032110

[43] Goodenough J B, Dabrowski B, and Zhou J S 2005 *Phys. Rev. Lett.* **95** 127204

[44] Canfield P C, Thompson J D, Cheong S W, and Rupp L W 1993 *Phys. Rev. B* **47** 12357

[45] Misra D and Kundu T K 2017 *J. Electron. Mater.* **46** 150

[46] Li J, Liu H F, Wu H W, Yang J C, Deng T, Liu S L, Xie R S, Guo B G, Zhang X Q, Zheng K, and Huo J C 2023 *Ceram. Int.* **49** 20723

[47] Moon E J, Gray B A, Kareev M, Liu J, Altendorf S G, Strigari F, Tjeng L H, Freeland J W, and Chakhalian J 2011 *New J. Phys.* **13** 073037

[48] Hua E, Si L, Dai K, Wang Q, Ye H, Liu K, Zhang J, Lu J, Chen K, Jin F, Wang L, and Wu W 2022 *Adv. Mater.* **34** 2206685

[49] Lu J, Si L, Zhang Q, Tian C, Liu X, Song C, Dong S, Wang J, Cheng S, Qu L, Zhang K, Shi Y, Huang H, Zhu T, Mi W, Zhong Z, Gu L, Held K, Wang L, and Zhang J 2021 *Adv. Mater.* **33** 2102525

[50] Sánchez-Santolino G, Rouco V, Puebla S, Aramberri H, Zamora V, Cabero M, Cuellar F A, Munuera C, Mompean F, Garcia-Hernandez M, Castellanos-Gomez A, Íñiguez J, Leon C, and Santamaria J 2024 *Nature* **626** 529

[51] Han L, Addiego C, Prokhorenko S, Wang M, Fu H, Nahas Y, Yan X, Cai S, Wei T, Fang Y, Liu H, Ji D, Guo W, Gu Z, Yang Y, Wang P, Bellaiche L, Chen Y, Wu D, Nie Y, and Pan X 2022 *Nature* **603** 63